

# A One-Pot Universal Approach to Fabricate Lubricant-Infused Slippery Surfaces on Solid Substrates

Alexander B. Tesler,\* Lucia H. Prado, Marat M. Khusniyarov, Ingo Thievesten, Anca Mazare, Lena Fischer, Sannakaisa Virtanen, Wolfgang H. Goldmann, and Patrik Schmuki\*

Wetting is a surface phenomenon that commonly occurs in nature and has an enormous influence on human life. Slippery liquid-infused porous surfaces have recently been developed to support the growing demand for anti-fouling coatings. While short-chain fluorinated compounds, commonly used to reduce the surface energy of substrates, are banned due to environmental toxicity, silane-based compounds are expensive and barely scalable. In this sense, silicone-based chemistry may match the gap as a real alternative. However, the grafting approaches demonstrated so far suffered from either slow binding kinetics or are applied under harsh conditions. Here, it is demonstrated that polydimethylsiloxanes graft to virtually any substrate when illuminated by UV light serving simultaneously as a reducing surface energy agent and infusing lubricant. This procedure is applied on metals, metal oxides, and ceramics of various surface morphologies. The proposed approach is simple, fast, scalable, environmentally friendly, and of low-cost, yet forms stable lubricant-infused slippery surfaces by a one-pot process. Due to the biocompatibility of silicone-based compounds, the process is examined on plain medically applicable substrates such as scalpel blades and glass lenses that display enhanced corrosion resistance, reduced friction through incision, and repel blood staining and bacterial adhesion without deteriorating their mechanical and optical characteristics.

controls the dynamics of adhesion on wet substrates such as mushroom spores and living cells.<sup>[2]</sup> In industry, corrosion, which is a pure surface phenomenon, occurs almost in all circumstances, where water-based liquids are in contact with solid material. The annual global cost of corrosion alone is estimated to be  $3.0 \times 10^{12}$  USD, which is equal to  $\approx 3.4\%$  of the global gross domestic product of the developed world.<sup>[3]</sup> Another vital example is the accumulation of unwanted material on solid surfaces that deteriorate their functionality named fouling. The fouling materials consist of either living organisms (i.e., biofouling) or non-living inorganic and/or organic compounds (i.e., chemo-fouling). It is estimated that  $\approx 3.1 \times 10^9$  USD are annually spent to remove biofouling invasion by clogging pipelines in industrial plants, while the control of fouling by water intake, piping systems, and heat exchangers of desalination membranes and power plants amounts to  $\approx 1.5 \times 10^{10}$  USD annually.<sup>[4]</sup> Furthermore, one of the most significant economic impact of fouling affects the shipping industry by substantially increased drag

on a ship's hull resulting in the reduction of the overall hydrodynamic performance of the vessel and an enormous rise in fuel consumption, that is, environmental pollution.<sup>[5]</sup>

Several strategies have been developed to combat fouling. Inspired by the Lotus leaf architecture, superhydrophobic

## 1. Introduction

Surface wettability is one of the most important properties for various biological processes as well as in engineering and industrial applications.<sup>[1]</sup> For instance, in biology, wetting/dewetting

Dr. A. B. Tesler, L. H. Prado, Dr. A. Mazare, Prof. S. Virtanen, Prof. P. Schmuki  
Department of Materials Science and Engineering  
Institute for Surface Science and Corrosion WW4-LKO  
Friedrich-Alexander University Erlangen-Nuremberg  
Martensstrasse 7, Erlangen 91058, Germany  
E-mail: alexander.tesler@fau.de; schmuki@ww.uni-erlangen.de

 The ORCID identification number(s) for the author(s) of this article can be found under <https://doi.org/10.1002/adfm.202101090>.

© 2021 The Authors. Advanced Functional Materials published by Wiley-VCH GmbH. This is an open access article under the terms of the Creative Commons Attribution-NonCommercial License, which permits use, distribution and reproduction in any medium, provided the original work is properly cited and is not used for commercial purposes.

DOI: 10.1002/adfm.202101090

Prof. M. M. Khusniyarov  
Department of Chemistry and Pharmacy  
Friedrich-Alexander University Erlangen-Nuremberg  
Egerlandstrasse 1, Erlangen 91058, Germany  
Dr. I. Thievesten, L. Fischer, Prof. W. H. Goldmann  
Department of Physics  
Biophysics Group  
Friedrich-Alexander University Erlangen-Nuremberg  
Henkestrasse 91, Erlangen 91052, Germany  
Prof. P. Schmuki  
Chemistry Department  
Faculty of Sciences  
King Abdul-Aziz University  
Jeddah 80203, Saudi Arabia

surfaces (SHS) emerged as a potential solution to creating self-cleaning antifouling surfaces.<sup>[6]</sup> However, the “Achilles heel” of such surfaces is their poor mechanical and pressure stability of the hierarchical micro/nano-scaled surface topography that is essential for obtaining very high water contact angles (WCA).<sup>[7]</sup> Furthermore, the metastable nature of the plastron layer limits SHS in their potential real-life application.<sup>[6,8]</sup> Despite substantial efforts developing artificial SHS, their applications are still rare.<sup>[7b]</sup>

Slippery liquid-infused porous surfaces (SLIPS) have recently been introduced as an alternative approach to conventional SHS.<sup>[9]</sup> Inspired by the *Nepenthes* plant, the slippery surface concept is based on the infusion of a porous substrate with a lubricating fluid that has a strong chemical affinity to the underlying substrate creating a stable, inert, and extremely smooth lubricant overlayer on the surface. This novel technology can effectively repel aqueous and organic liquids, microorganisms, insects, and ice, making it suitable for a wide range of applications.<sup>[10]</sup> The premise of slippery coatings is that a liquid surface is intrinsically smooth and defect-free down to the molecular scale thus reducing drag and the strength of adhesion of contaminants.<sup>[11]</sup> SLIPS function under high-pressure conditions, provide self-healing of imperfections, show optical transparency, reduce ice nucleation, and are ultra-repellent to complex fluids such as crude oil and brine<sup>[12]</sup> as well as repel highly contaminating biological media such as blood or biofilms during a brief exposure.<sup>[9b,10a,b,d,e,g,h,11,13]</sup>

There are several approaches to fabricate liquid-infused slippery surfaces. In general, SLIPS consists of three parts: i) a structured rough substrate, ii) an appropriate low surface energy coating, and iii) a low-surface-tension fluid frequently called lubricant.<sup>[14]</sup> So far, a variety of materials such as metals,<sup>[10g,12,13c,15]</sup> polymers,<sup>[10c,16]</sup> fabrics,<sup>[17]</sup> ceramics,<sup>[10h,18]</sup> to name a few, have been structured to fit the nanometer-scale roughness requirement.<sup>[19]</sup> However, only a few approaches have been adopted to reduce the surface energy of these substrates, utilizing mostly hydrocarbon- or fluorinated chains with silane-<sup>[10h,18a,20]</sup> or phosphate-based functional binding groups.<sup>[10g,11,13c,d,19,21]</sup> However, silane-based molecules are expensive and the process is complicated, thus making the functionalization processes barely scalable. On the contrary, short-chain perfluoroalkyl chemicals, which are unpretentious in use with low surface tension values matching well the SLIPS requirements, are subjected to the global regulation due to their environmental and human toxicity issues.<sup>[22]</sup> In this sense, non-fluorinated silicone-based materials are widely used in everyday life and a broad range of industrial applications including medical technology, construction, automotive, food packaging, and paper industry.<sup>[23]</sup> They are colorless, non-toxic, environmentally friendly,<sup>[24]</sup> and biocompatible,<sup>[25]</sup> have good thermal stability and excellent water repellency due to the organic-inorganic structure of siloxane molecules.<sup>[26]</sup>

Several approaches have been developed to graft silicones to solids. Polydimethylsiloxanes (PDMS), the most common silicone material, is usually grafted thermally on oxide surfaces.<sup>[27]</sup> However, thermal grafting is a harsh, time-consuming, and expensive process not readily applicable to various materials. Recently, it was demonstrated that methyl-terminated PDMS can spontaneously bind to glass at room temperature, while the dissociation kinetics is extremely slow to form a high-quality coating ( $\approx 100$  h).<sup>[26]</sup> Another approach is to use UV light in the

presence of a photocatalyst or crosslinker, which can be either added to the PDMS mixture<sup>[18b]</sup> or applied on nanostructured photocatalytic substrates such as TiO<sub>2</sub> or ZnO.<sup>[28]</sup>

This study, however, proves that UV illumination can induce photo-dissociation of specific bonds in PDMS molecules followed by their grafting to oxide surfaces in the absence of any photo-responsive catalyst. We demonstrate a way to create hydrophobic and lubricant-infused slippery surfaces by grafting bare PDMS oil to non-photoactive solid substrates. Using UV light, PDMS oil dissociates without the need of a photocatalyst, then grafts to virtually any surface. In this way, the PDMS serves both as i) reducing surface energy agent and ii) lubricating oil, minimizing the interfacial energy between the solid substrate and lubricant.<sup>[9b]</sup> The procedure is environmentally friendly, easy to implement, fast, scalable, and extremely low-cost. Solid surfaces such as ceramics (glass, quartz, and silicon wafers), metals (Al, Cu, steel, Co, Mo), and their oxides of various dimensions and morphologies from flat to rough, and porous can be coated to form hydrophobic and lubricant-infused slippery surfaces in an one-pot process. Silicone oils of various viscosities were applied to yield 5–12 nm thick high-quality UV-grafted coatings. The reaction kinetics is fast forming the slippery silicone layer within 15 min of illumination. The coated surfaces exhibit excellent corrosion protection for metals, repel complex liquids such as blood, reduce friction as well as substantially improve resistance to bacterial attachment when UV-grafted onto medically applicable substrates such as carbon- and stainless steel as well as glass lenses without deteriorating their mechanical and optical characteristics.

## 2. Results and Discussion

### 2.1. Physicochemical Characterization of UV-Grafted PDMS Layers

**Figure 1a** shows the schematic representation of the UV-grafted PDMS-infused slippery surface formation process. The coating was first applied on bare Si wafers. The substrates were cleaned ultrasonically in acetone and ethanol and then dried under a stream of N<sub>2</sub>. These samples display the WCA of  $48 \pm 1^\circ$  (Figure 1b). The cleaned samples were then placed horizontally on a Pyrex petri dish and a thin layer of silicone oil was dropped on the substrates allowing it to spread over the entire sample surface. The samples were illuminated by UV light at various time points from 5 to 60 min resulting in the formation of PDMS-infused slippery surfaces. To study the UV-grafted PDMS layers, the remnant oil was removed by an extensive rinse in toluene,<sup>[28a]</sup> followed by a wash in ethanol, and dried under a stream of N<sub>2</sub>. Since silicone oil is a sticky substance, the remnant oil, as well as unbound molecules, should be properly washed away. The stains of excessive oil can easily be observed on flat Si and Si/SiO<sub>2</sub> wafers by the appearance of a thin-film interference pattern (Figure S1, Supporting Information), while on the other samples, that is, polished metals and transparent glasses, cannot be easily detected. The UV-grafting reaction yields a 6–9 nm thick coating as a function of UV illumination time on a flat Si wafer by ellipsometry measurements using 500 cSt PDMS oil (Figure 1c). As shown, the plain Si wafer is hydrophilic due to the native oxide with a thickness of  $\approx 1.82 \pm 0.03$  nm correlating well with the

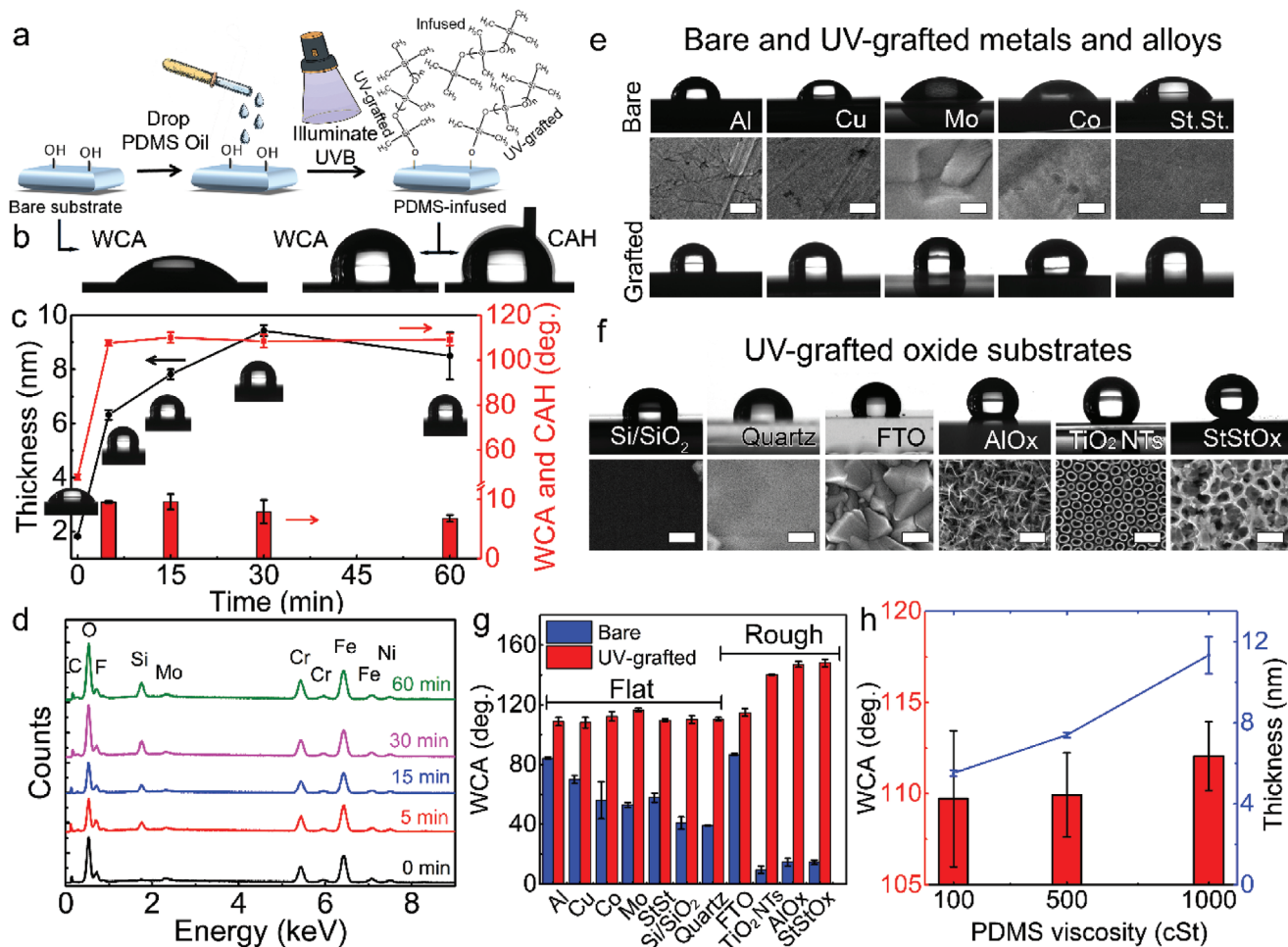


**Figure 1.** a) Schematic representation of the PDMS grafting procedure to form PDMS-infused slippery surfaces. b) The WCA of a bare silicon wafer (left image), and WCA and CAH of PDMS grafted Si wafer (the glow around the water drop in the right image represents the CAH obtained by the overlap between advancing and receding WCA images at 50% transparency). c) The PDMS layer thickness and corresponding WCA (red line) and CAH (red bars) values as a function of time of UV light illumination grafted on Si wafer. Insets: images of actual water drop shape on the UV-grafted Si wafer. d) EDX analysis of UV-grafted PDMS on polished stainless steel substrates as a function of UV light illumination time. Insets: images of actual water drop shape on the UV-grafted Si wafer. e) The WCA of bare (top row), PDMS-grafted (bottom row), and corresponding SEM images (middle row) of metallic substrates (from left to right): polished Al and Cu, bare Mo and Co, and polished stainless steel. f) The WCA and corresponding SEM images of PDMS UV-grafted oxide surfaces (from left to right): 100-nm-thick SiO<sub>2</sub> layer on Si wafer, quartz, pseudoboehmite alumina (AlO<sub>x</sub>), FTO, highly ordered TiO<sub>2</sub> nanotubes (TiO<sub>2</sub> NTs), and sponge-like anodized 316L grade stainless steel (StStOx). The scale bar in (e,f) for all HR-SEM images is 100 nm. g) WCA was measured before and after UV grafting of PDMS on the samples shown in (e,f), and h) WCA and layer thickness measured by ellipsometry of grafted PDMS layers on Si wafer with increased PDMS oil viscosity.

literature.<sup>[29]</sup> Once UV-grafted and rinsed in toluene, Si wafers turn hydrophobic displaying the WCA of  $106 \pm 1^\circ$  and a contact angle hysteresis (CAH) of  $\approx 10^\circ$  after only 5 min of UV light irradiation (Figure 1b). Between 5 and 60 min of the illumination, WCA does not change significantly, while CAH is slightly decreasing (Figure 1c). The WCA values achieved in this study are in agreement with reported values on flat substrates.<sup>[27d]</sup> The overall thickness of the grafted PDMS layer increases steadily up to 30 min of illumination then remains constant well within the standard deviation. This trend was also confirmed by EDX measurements (Figure 1d and Table S1, Supporting Information). The latter results may be attributed to the higher order (formation of a denser layer) of the grafted PDMS molecules rather than to the linear growth of attached molecules as previously shown by water-assisted PDMS-grafting.<sup>[26]</sup>

The PDMS grafting procedure can be applied virtually to any material. Here, we examined the following substrates: i) plain Si, and ii) Si wafer covered by 100-nm-thick SiO<sub>2</sub> layer, iii) 1-mm-thick standard microscope glass slides, 0.4-mm-thick borosilicate glass coverslips, and fluorine-doped tin oxide (FTO) conductive glass, and quartz, iv) bare Co, v) Mo foils, vi) polished Al, and Cu, vii) vertically aligned highly ordered anodized TiO<sub>2</sub> nanotubular arrays (TiO<sub>2</sub> NTs),<sup>[30]</sup> and viii) anodized 316L grade stainless steel with sponge-like nanoporous structure (Figure S2, Supporting Information). The WCA measured on flat and rough substrates was hydrophilic for all plain samples (Figure 1e,f). The grafted samples show the WCA as a function of the surface roughness (Figure 1g). All flat grafted samples demonstrate a WCA in the range of  $110 \pm 4^\circ$ , while rough substrates display  $115 \pm 3^\circ$ ,  $140 \pm 1^\circ$ ,  $147 \pm 3^\circ$ , and  $148 \pm 3^\circ$  for FTO,

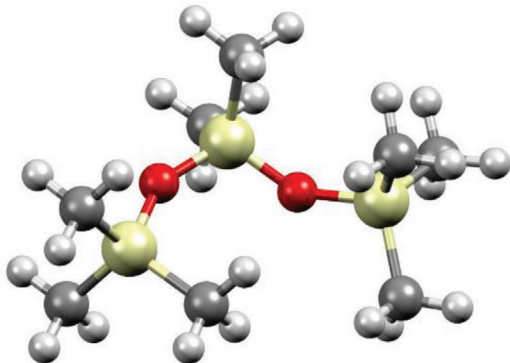
TiO<sub>2</sub> NTs, pseudoboehmite aluminum oxide, and anodized stainless steel, respectively.

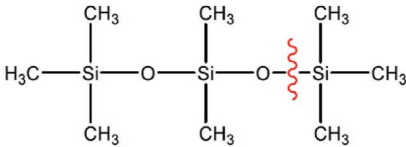
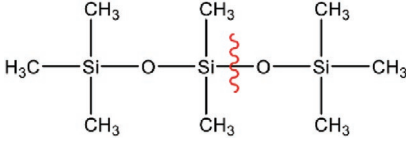
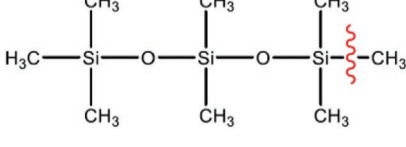
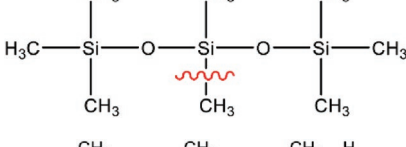
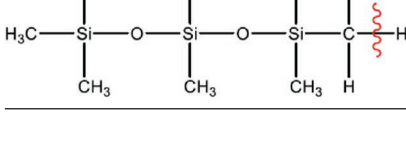
The influence of PDMS oil with increased viscosity on the wetting characteristics of the UV-grafted surfaces was studied on flat Si substrates. The overall thickness of the grafted PDMS layer increases with a rise in PDMS oil viscosity from 5.5 ± 0.2 nm for 100 cSt (*M<sub>w</sub>* = 6.0 kDa) oil to 7.4 ± 0.1 nm and 11.3 ± 0.9 nm for 500 cSt (*M<sub>w</sub>* = 173 kDa) and 1000 cSt (*M<sub>w</sub>* = 28 kDa), respectively. However, only a minor increase in WCA with an increase in oil viscosity was observed (Figure 1h). However, the obtained UV-grafted PDMS layer thicknesses differ substantially from the water-assisted and photo-catalytically grafted procedures. For instance, Liu et al. demonstrated that UV-grafted PDMS on photocatalytic TiO<sub>2</sub> layer, the thicknesses of 2.2, 4.0, and 5.5 nm were obtained for 6.0, 173, and 28 kDa PDMS oils, respectively.<sup>[31]</sup> The grafted PDMS layer thickness was then displayed versus molecular weight using a log-log plot. A straight line with a slope of *H* = 0.43 ± 0.14 was obtained (Figure S3, Supporting Information). The grafting density can be calculated by  $\sigma = (H\rho N_A)/M_w$ , where  $\rho$  is the bulk density of polymer and *N<sub>A</sub>* is Avogadro's number.<sup>[31]</sup> Grafting densities of 5.3, 2.5, and 2.3 × 10<sup>17</sup> molecules per m<sup>2</sup> were obtained for 6.0, 173, and 28 kDa PDMS, respectively. These results correlate with the literature indicating that the higher *M<sub>w</sub>* PDMS molecules occupy a larger area, thus increase the barrier for the next arriving molecule and, by that, reducing the grafting density. Nevertheless, the grafting density obtained in this study is doubled compared to thermal PDMS-grafting,<sup>[27d]</sup> and to that obtained on photocatalytic TiO<sub>2</sub> substrates.<sup>[28a]</sup> The latter can be attributed to the non-specific dissociation of PDMS molecules occurring on the photocatalytic substrates, while in absence of photoactive material, this probability diminishes.

Several studies evaluated the photo-dissociation of silicon elastomers.<sup>[32]</sup> In these cases, however, UV light with  $\lambda < 254$  nm was utilized to prepare a permeable SiO<sub>2</sub> layer on cross-linked polysiloxanes, while we are interested in the induction of selective grafting processes. To address this issue, we performed density functional theory (DFT) calculations on a PDMS truncated model molecule Me<sub>3</sub>Si–O–SiMe<sub>2</sub>–O–SiMe<sub>3</sub> (Table 1). Bond-dissociation enthalpies for breaking the molecule at different positions into two fragments were calculated as a measure of probability for a dissociation process. According to calculations, the dissociation enthalpy for Si–Me bonds is the smallest, and thus these bonds are generally weaker and more likely to break. UV light  $\lambda < 321$  nm (UVB) is required for photo-dissociation. The Si–O bonds are the strongest, and, therefore, harder and less expected to break, while stronger UV light  $\lambda < 214$  nm (UVC) is required in this case (Table 1). Consequently, in the case of selective grafting using mild UV light, PDMS oil is expected to be activated at Si–Me bonds being grafted to surfaces via silicon. The typical spectrum of the medium pressure UV lamp used in this study is shown in Figure S4, Supporting Information. As shown, the highest intensity peaks are observed at  $\lambda = 320$  and 370 nm indicating that the lamp provides a sufficient amount of energy at  $\lambda = 321$  nm to dissociate Si–Me bonds.

To study the chemical composition as well as surface coverage of UV-grafted PDMS layers, angle-resolved X-ray photoelectron (XPS) spectroscopy analysis was performed at angles of 15, 45, and 75°, namely to control the detection depth in a sample by changing the sample's tilt angle. PDMS oils of 100, 500,

**Table 1.** Calculated bond dissociation energies and corresponding wavelengths required for dissociation of a Si<sub>3</sub>-truncated model of PDMS (silicone oil) at given locations. Theory level: DFT/M062X/def2-TZVP, zero-point, and thermal energy corrections have been applied.



Molecular structures with bonds to be dissociated	Bond dissociation enthalpy <i>DH</i> <sup>0</sup> <sub>298</sub> , [kcal mol <sup>-1</sup> ]	The appropriate wavelength for dissociation, [nm]
	133.5	214
	138.5	207
	89.0	321
	90.4	317
	96.5	296

and 1000 cSt viscosity have been grafted on polished 316L grade stainless steel substrates, and the typical high-resolution XPS spectra are shown in Figure 2a–d and (Figure S5a,b, Supporting Information). An austenitic stainless steel alloy was measured as a reference showing the typical Fe, Cr, Ni, Mo, O, and C peaks (Figure S6a,b, Supporting Information).<sup>[33]</sup> When UV-grafted, the survey XPS spectra consist of Si, O, and C peaks associated with PDMS, while the Fe 2p peak arising from

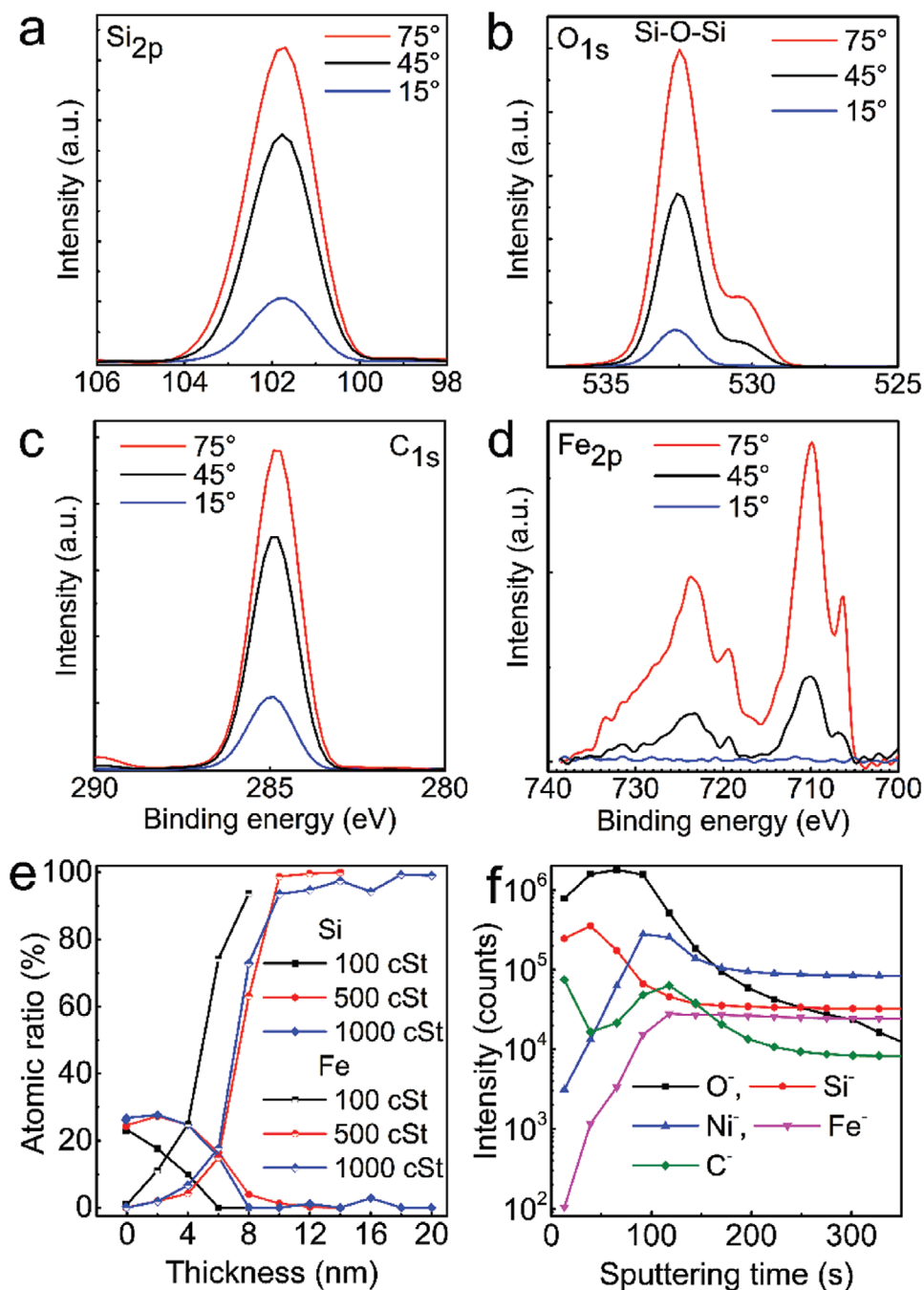


**Figure 2.** High-resolution angle-resolved XPS spectra of UV-grafted 100 cSt PDMS oil on polished stainless steel substrates: a) Si 2p, b) O 1s, c) C 1s, and d) Fe 2p. e) XPS depth profile of Si and Fe UV-grafted PDMS oil of various viscosities on polished stainless steel substrates. f) ToF-SIMS depth profile of secondary ions derived from 100 cSt PDMS oil UV-grafted on polished stainless steel. The y-axis is in logarithmic scale.

the substrate is barely noticeable (Figure S6a, Supporting Information). Still, the Fe 2p peak is clearly shown in the high-resolution XPS spectrum measured at 75° angle, and it completely disappears at 15° angle confirming that the PDMS grafted layer covers the substrate entirely (Figure 2d). The high-resolution Si 2p XPS spectrum consists of a single peak at the binding energy of 102.2 eV (Figure 2a), which can be deconvoluted into two components: at 102.2 eV (35%) and 102.8 eV (65%) corresponding to Si–C and Si–O bonds, respectively (Figure S7a,

Supporting Information).<sup>[34]</sup> In the case of the O 1s spectra, the main peak centered at 532.6 eV, and a shoulder at 530.5 eV is clearly visible. This shoulder is highest at 75° angle (Figure 2b, red spectrum), and disappears at angle of 15° (Figure 2b, blue spectrum). Further deconvolution of the O 1s peak at 75° angle of the 100 cSt UV-grafted PDMS, leads to three components: at 532.6 eV (83.5%) corresponding to the Si–O–Si bond,<sup>[35]</sup> and 531.1 eV (2.1%), and 530.3 eV (14.4%) corresponding to Me–O–Si and Me–O–Me bonds, respectively, where Me

represents Fe, Ni, or Cr, that is, main components of the substrate (Figure S7c, Supporting Information).<sup>[28a]</sup> When measured at a 15° angle, only two components are observed: 532.6 eV (98.1%) and 530.3 eV (1.9%) assigned for Si—O—Si and Me—O—Me bonds, respectively, that is, the peak attributed to Me—O—Si disappears (Figure S7d, Supporting Information). The latter results indicate again a complete coverage of the surface by the grafted PDMS molecules. A similar tendency was also observed for the higher molecular weight PDMS UV-grafted to stainless steel substrates, whilst the Me—O—Me peak was barely noticeable even at 75° angle (Figure S5, Supporting Information). The C 1s spectra display a single peak at 285.0 eV, which is associated with Si—C bonds in PDMS oil (Figure 2c, and Figure S6a, Supporting information).<sup>[36]</sup> Furthermore, the Si and Fe XPS sputter profiles of UV-grafted PDMS oil of various viscosities demonstrate that the thickness of the grafted PDMS layers increases with oil viscosity (Figure 2e), correlating well with ellipsometric measurements (Figure 1h).

Time of flight secondary ion mass spectrometry (ToF-SIMS) analysis was performed for the UV-grafted PDMS layers deposited on AISI 316L grade stainless steel substrates, and the results are summarized in Figure 2f and Figure S8, Supporting Information. The positive and negative spectra confirm the coverage of the surface by PDMS layer, as typical mass peaks are observed for PDMS,<sup>[36]</sup> for example, with positive polarity +43, +73, +147, +207 amu (Figure S8a,b, Supporting Information). A difference in the Si<sup>+</sup>, O<sup>-</sup>, Si<sup>-</sup> mass fragment intensities is also observed for the UV-grafted PDMS layers with different viscosities (Figure S8c, Supporting Information).

To further investigate the UV-grafted PDMS layer, negative depth profile obtained by ToF-SIMS analysis of the UV-grafted 100 cSt PDMS oil for selected representative fragments (C<sup>-</sup>, O<sup>-</sup>, Si<sup>-</sup>, Ni<sup>-</sup>, and Fe<sup>-</sup> signals) is presented in Figure 2f. The depth profile is listed as signal intensity for the sputtering time, since converting the sputtering time of ToF-SIMS into depth is difficult as the sputtering rate depends on the material; thus the sputtering time serves as a qualitative measure of depth.<sup>[37]</sup> The interface between the PDMS layer and the substrate is reached at ≈140 s, as after this time the increasing intensity of the Fe<sup>-</sup> and Ni<sup>-</sup> signals reaches a plateau, that is, sputtering of the substrate sample. The Si<sup>-</sup> signal is representative of the PDMS layer, and the intensity of Si<sup>-</sup> initially increases during the first 40 s, then decreases continuously till 140 s of sputtering, and a steady-state value is reached (Si is present in the austenitic grade steels as impurity). The intensity of O<sup>-</sup> and C<sup>-</sup> is more complex as the concentration of O<sup>-</sup> initially increases for 60 s of sputtering, and then decreases continuously (due to the native oxide layer), while for C<sup>-</sup> it decreases for 40 s and then starts increasing (a bump at 120 s of sputtering) and, finally, reaches a steady condition at 300 s. The latter may be explained by the presence of carbon in the austenitic grade stainless steel substrate. The initial low intensities of Fe<sup>-</sup> and Ni<sup>-</sup> corroborate the high coverage of the solid substrate by the UV-grafted PDMS layer. In particular, the variance in the intensities of C<sup>-</sup>, O<sup>-</sup>, and Si<sup>-</sup> signals can point to the preferential orientation of the low viscosity UV-grafted PDMS molecules on the solid substrate, while the top trimethylsiloxane group is initially removed exposing O and Si atoms. Our XPS and ToF-SIMS analysis confirm the formation of the UV-grafted PDMS layers; yet, further research is

required to investigate the detailed structure and orientation of the PDMS UV-grafted layers of various molecular weights.

## 2.2. Corrosion Resistance of UV-Grafted PDMS on Metallic Substrates

Corrosion is a natural process of metal deterioration, driven by its reaction to the surrounding environment, and is the main reason for the failure of metal structures. The need to minimize the damage caused by corrosion is particularly evident when it comes to engineering materials such as Al, Cu, and various grades of steel. It was previously demonstrated that hydrophobic fluorinated surfactants can form a strong and stable covalent bond with the native or anodized oxide layers forming a self-assembly monolayer coating to reduce surface wettability and, thereby, inhibiting the corrosion of the protected metal.<sup>[38]</sup> However, due to environmental issues, the use of such fluorinated surfactants is now limited; therefore, alternative materials and methods should be developed. In this sense, the hydrophobic PDMS coating can protect metallic substrates against corrosive media, being non-toxic to the surrounding environment.

As an example, we evaluated the corrosion resistance of plain, UV-grafted, and PDMS-infused flat Al substrates by dropping 1 M NaOH aqueous solution on their surfaces. The plain and UV-grafted samples react almost immediately with the corrosive solution, while the PDMS-infused sample displays a ≈10 min delay in the corrosion initiation being comparable with the thermally grafted PDMS layers.<sup>[27d]</sup> After that time, H<sub>2</sub> bubbles corresponding to H<sup>+</sup> cathodic reduction appear also on the PDMS-grafted sample, yet the etching solution preserves its drop shape restricting the fast spreading of the corrosive media over the entire sample surface (Figure S9a, Supporting Information). After 15 min, the corroded area fraction was calculated and found to be 96%, 43%, and 18% for the plain, UV-grafted, and PDMS-infused Al, respectively (Figure S9b, Supporting Information). Such a facile dropping test demonstrates not only a delay in corrosion initiation of the PDMS-infused samples but also limits the spreading of the corrosive medium on the PDMS-infused surface indicating robust corrosion resistance.

As a next step, we performed standard potentiodynamic polarization measurements for Al, Cu, and AISI 316L grade stainless steel. Potentiodynamic polarization curves in **Figure 3** display the corrosion behavior in a standard 3.5 wt% NaCl electrolyte solution. The corrosion susceptibility decreases when stainless steel, Al, and Cu substrates are UV-grafted with PDMS oil. Stainless steel and Al show a passive behavior until the onset of pitting corrosion, which is increased toward higher potentials after the surface grafting. Cu shows active dissolution starting with an activation-controlled region followed by a diffusion-controlled plateau with higher current densities. The corrosion potential of the three materials is increased, while the corrosion current is at least one order of magnitude lower in the case of stainless steel and Cu. On the other hand, Al shows the presence of metastable pitting until the onset of pitting corrosion is reached.

The effect of UV-grafted PDMS layer on the corrosion of metal substrates was quantified by the potentiodynamic polarization measurements. The corrosion current densities ( $I_{corr}$ ) were estimated using Tafel plots, and the results are summarized in

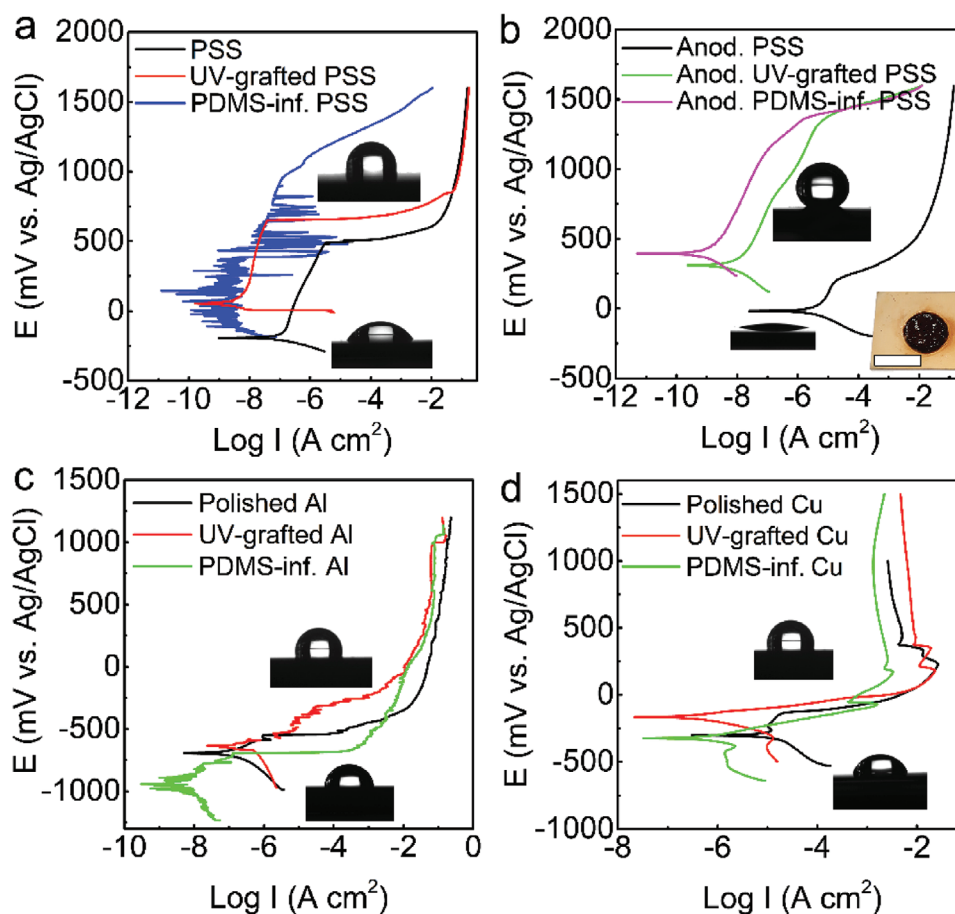


**Figure 3.** Potentiodynamic polarization curves in 3.5 wt% NaCl electrolyte of a) polished bare (PSS, black), PDMS UV-grafted (red), and PDMS-infused (blue) 316L-grade stainless steel, b) anodized bare (black line), anodized PDMS UV-grafted (green) and anodized PDMS-infused (magenta) 316L-grade stainless steel, c) polished bare (black), PDMS UV-grafted (red), and PDMS-infused (green) Al, and d) polished bare (black), PDMS UV-grafted (red), and PDMS-infused Cu. Inset images show WCA on the bare and UV-grafted samples used for the corrosion experiments. Inset in (b): digital image of the as-anodized stainless steel sample after potentiodynamic polarization experiment. The bright whitish pits indicate localized dissolution of the anodized oxide layer exposing the underlying metallic substrate. The scale bar of the inset image is 1 cm.

Figure 3 and Table S2, Supporting Information. The corrosion current density of the UV-grafted steel is one order of magnitude lower than that of bare steel (Figure 3a). This indicates that the grafting of PDMS coating suppresses the corrosion of stainless steel with a corrosion inhibition efficiency (IE) of 96.8%. Lubricant-infused slippery samples fabricated by grafting a PDMS layer and without removing the remnant oil showed an even higher corrosion resistance. The noisy signal near the open circuit potential (OCP) in both, cathodic and anodic range, is given by the low current density, with values near the equipment scale limit. The passive current density values are similar to the UV-grafted substrate. Also, when a potential near the pitting potential of the bare substrate is reached, current spikes start to appear until the onset of pitting corrosion at circa 1.0 V. The fact that these spikes reach such high current values indicate that localized events similar to metastable pitting corrosion could take place, but in this case, instead of re-passivation, a self-healing effect of the liquid coating occurs covering these sites, hence lowering the current until a new location is attacked.

Potentiodynamic polarization of bare anodized stainless steel in the chloride-containing electrolyte shows a higher  $I_{corr}$  a

lower  $E_{corr}$  and a shorter passivation range due to the onset of pitting corrosion when compared to the bare stainless steel substrate (Figure 3b and Table S2, Supporting Information). Pitting corrosion was also evident by the localized dissolution of the anodized oxide layer, while the underlying metallic substrate could be observed (Figure 3b, inset). Corrosion behavior of anodized stainless steel substrates has been previously reported.<sup>[39]</sup> However, the anodized and UV-grafted substrate presented a strong decrease in both  $I_{corr}$  and  $E_{corr}$ . When the anodized stainless steel samples were further infused by PDMS lubricant, an additional order of magnitude decrease of the corrosion current density is observed in comparison to the anodized UV-grafted steel (Figure 3b). Thus, both PDMS coated samples demonstrate almost 100% corrosion IE compared to the bare anodized stainless steel substrate. Furthermore, the passivation range was once again increased, proving that the grafted PDMS layer and the infused coating highly decrease the susceptibility to pitting corrosion. A similar trend was also observed in medical-grade instruments made of martensitic stainless and carbon steel, which is prone to corrode in saline solutions. As we show below, the corrosion resistance of the UV-grafted carbon

grade steel blades improves substantially, while its plain analog corrodes almost immediately, when both were exposed to the corrosive bacteria culture medium consisting of 0.1 wt% NaCl.

Finally, we examined corrosion resistance of Al and Cu, widely used in industrial applications metals, which are prone to corrode when exposed to corrosive chemicals. The Cu substrate UV-grafted with PDMS oil demonstrated a corrosion IE of 94.8%, while the corrosion current of the Al UV-grafted sample was at the same level as the bare Al substrate. When infused with silicone oil, the same samples show 98.1% and 99.9% corrosion IE for Al and Cu, respectively. Here, the addition of silicone lubricant forms a homogeneous thin layer on the UV-grafted PDMS layer due to the matching surface energies that serves as a passivation layer inhibiting direct contact between the corrosive media and the solid substrate. As shown, the coating process can be efficiently applied on various plain metal surfaces without porous structuring or other pre-treatments. However, as demonstrated by potentiodynamic diagrams, the porous PDMS-infused surfaces demonstrate an additional enhancement in the corrosion resistance, while micro/nano-structuring of the substrate certainly compromises its mechanical characteristics. Therefore, the compromise between surface structuring of the metal surface, that is, mechanical properties, and its corrosion resistance characteristics should be considered depending on the metal application requests.

### 2.3. PDMS UV-Grafted Process Applied on Medically Applicable Surfaces

Several materials are commonly used in medical devices, among them steel and glass, both of which often suffer from chemical and biological fouling. The process of biofouling is complex, but it starts with spontaneous non-specific adsorption of organic molecules on the surface followed by colonization of micro-organisms.<sup>[40]</sup> We<sup>[10g,11]</sup> and others<sup>[10a,27d]</sup> have recently demonstrated that SLIPS effectively repel adhesion of Gram-positive and Gram-negative bacteria such as *Escherichia coli*, *Staphylococcus aureus*, and *Pseudomonas aeruginosa*, which are of considerable medical importance due to their ubiquitous presence and multiple drug-resistance in humans. However, chemicals that are used to lower surface energy of solid substrates as well as lubricants, are commonly fluorinated compounds, while toxicity and relatively high-cost issues limit their application in the biomedical field.

The PDMS-based materials are promising candidates for practical anti-biofouling applications. PDMS is a low surface energy material that can be applied as a non-toxic alternative to antimicrobial, that is, antibiotic-based coatings, lowering the adhesion force acting between fouling organisms and the coating surface because of its low surface energy and small modulus.<sup>[24]</sup> However, PDMS grafting processes that have been presented so far suffer from either slow binding kinetics, that is, from several hours to days, or the application of harsh grafting conditions such as high-temperature thermal treatments. Therefore, a simple, rapid, low-cost, and robust process to modify the surface of medical devices of biocompatible material to reduce chemo- and biofouling without compromising their mechanical characteristics is of vital importance. Here, we performed

several tests to modify medically related substrates such as steel scalpel blades and glass lenses to verify their passive anti-biofouling resistance due to the UV-grafted PDMS coating.

#### 2.3.1. Blood-Repellent Properties of UV-Grafted PDMS Layers on Surgical Devices

Surgical blades can be manufactured from either carbon- or martensitic stainless steel (MSS), both of which have to comply with the requirements of BS 2982:1992 or BS EN ISO 7153 Part 1 standards that specify hardness and material composition.<sup>[41]</sup> This is to make sure that the blades are fairly corrosion-resistant, have a high degree of strength, shock-resistant, and in some particular cases are non-magnetic. Here, carbon steel blades offer a better combination of initial sharpness and durability, while at the same time they rust almost immediately when coming into contact with saline solutions (Figure S10, Supporting Information).<sup>[42]</sup> Therefore, we examined the influence of UV-grafted PDMS coating in both “as-grafted” and lubricant-infused configurations on the corrosion resistance blade grades using the potentiodynamic polarization technique.

Potentiodynamic polarization of plain carbon- (CS) and MSS scalpel blades, UV-grafted with PDMS oil and PDMS-infused show a clear decrease of corrosion susceptibility (Figure 4a,b and Table S3, Supporting Information). The carbon steel blade presents a higher corrosion potential and a decrease in corrosion current with a 69.5% corrosion IE in the case of CS blades grafted and further infused with PDMS oil. Furthermore, the onset of active dissolution is delayed toward higher potentials. The corrosion resistance of MSS blades is improved even further by the PDMS coatings. This could indicate a higher quality of the coating due to the hydroxide reach layer on the surface of the native passive oxide, which has more hydroxide bonds available to react with the PDMS molecules. MSS blades grafted with PDMS oil showed a 98.8% corrosion IE, whilst with MSS blades (grafted and infused) not only the corrosion potential of the blade is lower, but also the current density in the passive region, hence generating a noisy signal of  $10^{-9}$  A cm<sup>-2</sup>. Additionally, a significant delay in pitting corrosion onset is observed.

In invasive medical procedures, the scalpel blade surface experiences significant friction made through the skin and subcutaneous tissue incision. At the same time, these instruments are exposed to pathogens on the patient's skin and blood, potentially leading to infection.<sup>[10g]</sup> Therefore, the performance of the UV-grafted PDMS coating was evaluated first by making an incision with the treated blades into viscoelastic silicone rubber slabs of various softness and stickiness PDMS (base/curing agent ratios of 30:1, 20:1, and 10:1, SYLGARD 184) chosen to mimic skin tissues.<sup>[10g]</sup> This was followed by submersion into whole blood and medium containing *E. coli* and *S. aureus*.

In controls, that is, untreated scalpel, the softest slab (30:1) stuck to the scalpel surface and moves along the direction of the cut creating an uneven incision in both scalpel types (Figure 4c, top row). For the hardest slab (10:1), it was very difficult to cut through it because of the high friction. In all cases, incisions produced by untreated scalpels tend to have non-uniform cuts and

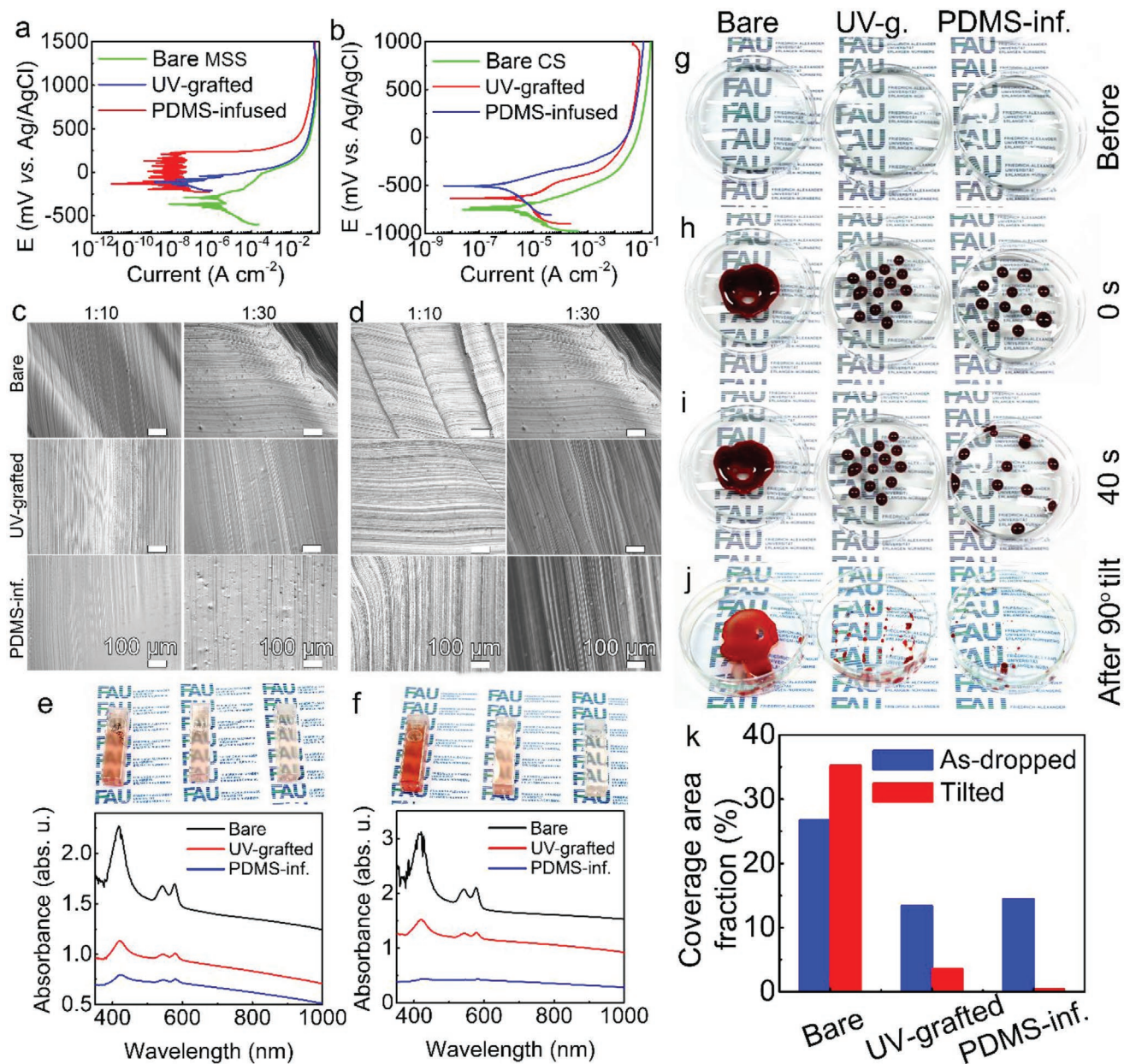


**Figure 4.** a,b) Potentiodynamic polarization of medical scalpel blade steel in 3.5 wt% NaCl electrolyte of bare, PDMS UV-grafted, and PDMS-infused made of a) MSS and b) carbon steel (CS). c,d) Optical microscope cross-sectional images of incisions produced on 1-cm-thick, sliced PDMS slabs with increased softness and stickiness (base/curing agent ratio, indicated) by untreated (top row), UV-grafted PDMS (middle row), and lubricant-infused slippery (bottom row) scalpel blades made of (c) carbon and (d) MSS. e,f) Digital still images and UV-Vis absorbance spectra of blood that adheres to the scalpel surface are shown in (a,b) after washing in PBS. g–i) Still digital images of bare, PDMS UV-grafted, and PDMS-infused double-convex glass lenses g) before, h) immediately after dropping, and after i) 40 s of exposure to 500  $\mu$ L fresh blood. j) Digital images of the lenses are shown in (g–i) after tilting by 90° to remove blood from the lens surface. k) Coverage area fraction of bloodstains on glass lenses calculated for each lens in as-dropped (h) and after tilting by 90° (j) states.

fractures due to the stick-slip-like, jerking motion as observed by the appearance of perpendicular lines periodical to the scalpel motion. In contrast, the UV-grafted and PDMS-infused blades produced nearly identical incisions on all slabs (Figure 4c,d, middle, and bottom rows), which are as smooth as the scalpel blade edge roughness (Figure S11, Supporting Information).

When medical devices come into contact with blood, the interaction poses a threat of undesired activation of blood cells

(platelets and monocyte/macrophages of the immune system) or other bioactive blood components (complements of coagulation cascades) potentially leading to the formation of blood clots, or thrombi, inflammation, or a more widespread, prolonged activation of the immune system.<sup>[7a]</sup> Therefore, after the incision experiments, treated and control scalpels of both grades were submerged in a cuvette with fresh blood (Figure 4e–f and Movies S1–S3, Supporting Information). After 10 s of

submersion, the scalpels were withdrawn from the cuvette with blood and washed in a cuvette filled with 4 mL of phosphate buffer saline (PBS). The amount of adherent blood to UV-grafted and PDMS-infused scalpels was substantially lower as indicated by the color of the cuvette filled with PBS and by UV-Vis spectroscopy (Figure 4e,f). The bare scalpels demonstrate a significant amount of attached blood in both cases as shown by the remaining blood on its surface and the pinned buffer film after the wash in PBS (see Movie S1, Supporting Information). The PDMS-infused scalpels display substantial reduction or even the absence of the peaks associated with hemoglobin (Figure 4e,f, blue spectra, and Movie S3, Supporting Information).<sup>[43]</sup> The superior blood repellent performance is attributed again to the existence of a stable liquid-liquid interface, formed between the low-surface-tension liquid and the blood, which is contrasted by the easily contaminated solid surface present of bare scalpels. The latter result is in good agreement with previously reported blood-repellent properties of SLIPS under static or flow conditions,<sup>[9b,10d,g]</sup> but this important anti-fouling characteristic can now also be applied on a bare non-porous substrate without compromising mechanical characteristics of bulk material. It should be, however, emphasized that even UV-grafted PDMS scalpel of both steel grades sustained their repellent characteristics after submersion in blood, demonstrating a decrease in adhesive blood (Figure 4e,f, black and red spectra, and Movie S2, Supporting Information).

Over the years, the field of optical instrumentation in biomedical applications has evolved due to the constantly growing demand for minimally invasive surgical procedures such as laparoscopy and diagnostic measurements such as endoscopy. While laparoscopic cholecystectomy rapidly became the standard of care for cholelithiasis after 1988, the use of minimally invasive techniques for other abdominal operations is yet limited.<sup>[44]</sup> Several inherent pitfalls of laparoscopy hinder the performance of these operations, including the limited motion of straight laparoscopic instruments, the narrow field of view, and poor visibility due to bleeding.<sup>[45]</sup> Surgical laparoscopes used for minimally invasive procedures consist of hollow tubes made of high-quality stainless steel that gradually developed to include fixed glass lenses for magnified vision.<sup>[46]</sup> Modern scopes are designed with multiple parts including a CCD camera, viewing, and energy-supply devices, and a lens cleaner to mechanically wipe off blood to improve the field of view. Several attempts have been made to create glass surfaces slippery, while in all these cases the surface was first roughened by micro/nano structures.<sup>[10h,18a]</sup> The latter, however, alternates dramatically the mechanical characteristics of the prepared slippery liquid-infused glass substrates. Once damaged due to the mechanical abrasion, which frequently occurs during the surgery, it would lose slipperiness further altering its blood-repellent characteristics.<sup>[10h]</sup> Therefore, considering that the structuring process is rather complicated and the mechanical robustness is weak, both these factors limit the future application of slippery liquid-infused porous glass surfaces in real devices.

As demonstrated above, various grades of steel can be UV-grafted by silicone oil, which prevents blood adhesion as well as making incisions smoother. The wetting characteristics were preserved on both structured and flat substrates without

deteriorating the mechanical characteristics. We applied therefore our PDMS UV-grafting procedure on the second functional component of the laparoscope that interacts with human tissue, that is, magnifying glass lenses to improve the field of view in a passive form, that is, without application of any external stimuli or energy (Figure 4g–k). Figure 4g shows bare (left lens), PDMS UV-grafted (middle lens), and PDMS-infused (right lens) lenses of comparable transparency. However, the wetting characteristics of bare, and UV-grafted or PDMS-infused lenses differ substantially (see Movie S4, Supporting Information). Fresh blood (500  $\mu$ L) was added dropwise on every lens. An increased amount of blood finally led to the percolation of individual droplets covering  $\approx$ 27% of the bare hydrophilic lens surface (Figure 4h,i, left lens). At the same time, UV-grafted and PDMS-infused samples, which are hydrophobic, prevent percolation of blood droplets, which cover only  $\approx$ 14% of the lens surface in both cases (Figure 4h, middle and right lenses). Nevertheless, there is a substantial difference also between the UV-grafted and PDMS-infused lenses. On the UV-grafted lens, blood remains static independently of the lens curvature (Figure 4i, middle lens), while it immediately slides off on the PDMS-infused lens. The sliding velocity depends on the curvature, as it takes  $\approx$ 40 s for the droplets to slide off completely from the top of the lens leaving behind a completely clear field of view (Figure 4j). Afterward, the lenses were tilted vertically to remove the blood, and the covered area fraction was calculated and found 35%, 3.58%, and 0.46% for the bare, UV-grafted, and PDMS-infused lenses, respectively (Figure 4k). The latter indicates that such a facile treatment of laparoscope functional surfaces can significantly improve its field of view without the image distortion as well as keeping its mechanical characteristics. Furthermore, the device can be mechanically wiped and chemically cleaned after the medical treatments, then re-grafted using the same procedure by simultaneously sterilizing it by intense UV-light illumination.

### 2.3.2. Anti-Bacterial Properties of UV-Grafted PDMS Layers on Surgical Devices

The second issue that should be considered in biomedical applications is the existence of various types of bacteria on the human skin. It is well-known that surgical site infections (SSIs) are among the most common healthcare-associated infections, which are associated with longer postoperative hospital stays, additional surgical procedures, treatment in intensive care, and higher mortality. The percentage of SSIs can vary from 0.5 to 10%, depending on the type of surgical procedure, while a statistically significant increasing trend was observed for both the percentage of SSIs and the incidence density of in-hospital SSIs following laparoscopic cholecystectomy in recent years.<sup>[47]</sup> Here, we examined the process of bacterial adhesion on steel substrates. To demonstrate the antibacterial characteristics of the UV-grafted surfaces, *E. coli* (Gram-negative) and *S. aureus* (Gram-positive) bacteria were cultured on bare, polished, UV-grafted, and PDMS-infused substrates as well as on anodized porous PDMS-infused steel substrates. These two types of bacteria are frequently found on human skin. All the substrates had a flat morphology without pores or textured structures

except the anodized ones. Initially, the samples were sterilized in a 70 vol% ethanol solution and then incubated in bacterial solutions to analyze bacterial attachment. After 24 h, the samples were withdrawn from the growing bacterial solution, gently

washed with DI water then stained by crystal violet dye.<sup>[48]</sup> The results are presented in **Figure 5a–l**. The surface coverage was calculated using bright-field microscopy in reflectance mode as shown in Figure 5a–j and backed up by confocal fluorescence

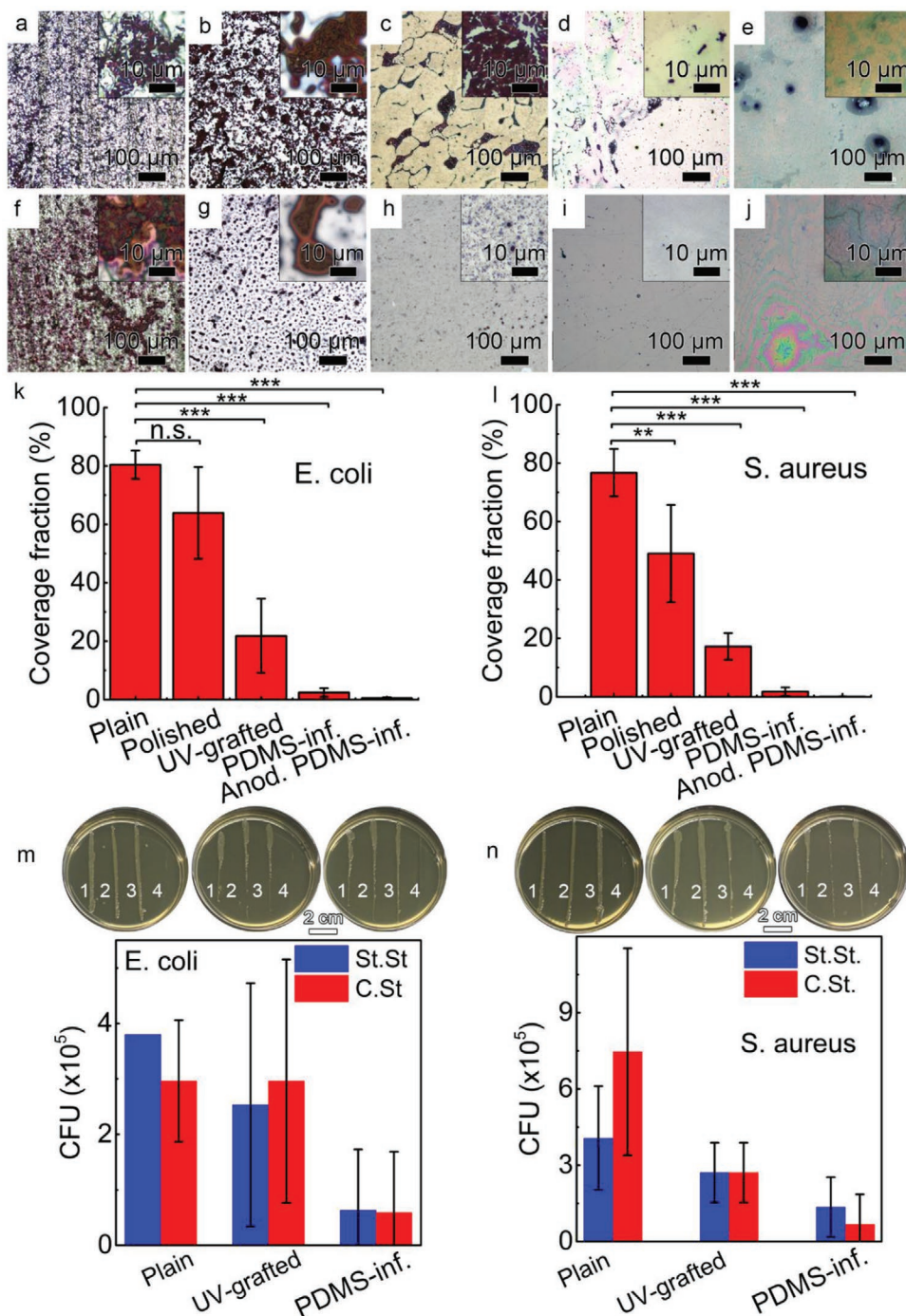


**Figure 5.** Bright-field reflectance images of a–e) *E. coli* and f–j) *S. aureus* adhering to austenitic stainless steel substrates with the following modifications: a, g) bare “as-received”, b, h) bare polished, c, i) polished UV-grafted, d, j) polished lubricant-infused, and e, k) polished-anodized, and lubricant-infused. k, l) Surface coverage area fraction calculated from the optical microscope images for all samples. Triplets were used for statistical analysis and at least two independent images were imaged of every sample. m, n) Colony-forming unit counts for bare, UV-grafted, and PDMS-infused scalpel blades after dipping in a tryptic soy broth medium containing *E. coli* or *S. aureus* followed by extensive rinsing. Insets in (m, n) are representative images of the agar Petri dishes with incisions made by the bare, UV-grafted, and lubricant-infused scalpel blades. Scalpel blades (1–3) were used for every treatment, while the incision (4) was made by sterilized in 70 vol% ethanol solution scalpel blades.

microscopy and SEM imaging (Figures S12 and S13, Supporting Information). As shown, both bacteria biofilms are formed on bare and polished steel substrates resulting in purple color over their entire surface due to crystal violet staining. The surface coverage of the bare hydrophilic steel substrates was estimated as  $80 \pm 5\%$  and  $78 \pm 8\%$  for *E. coli* and *S. aureus* biofilms, respectively; on the polished steel samples it was reduced to  $64 \pm 16\%$  for *E. coli* ( $p = 0.082$ ) and  $49 \pm 17\%$  for *S. aureus* ( $p = 0.030$ ) biofilm coverage (Figure 5a,b,f,g). According to the SEM images, the formed biofilms consist mainly of a single layer of bacteria (Figure S13a,c, Supporting Information). The UV-grafted PDMS samples already revealed a significant reduction in the biofilm surface coverage displaying  $22 \pm 13\%$  and  $17 \pm 5\%$  for *E. coli* and *S. aureus*, respectively ( $p < 0.005$ ). There are, however, substantial differences in the biofilms formed on the UV-grafted substrates. According to the SEM images, biofilms formed on the UV-grafted samples consist of multilayer structures (Figure S13b,d, Supporting Information). This difference is attributed to considerably weaker adhesion of both types of bacteria to the grafted surface, while the drug applied by the capillary force due to the evaporation of water is enough to detach bacteria from the substrate and condense them into multilayered clusters. At the same time, the PDMS-infused samples exhibit outstanding resistance against bacteria inhibiting almost complete adhesion of biofilms to the substrate surface ( $p < 0.005$ ) (Figure 5d,e,i,j). The attachment and biofilm formation for the *E. coli* and *S. aureus* are suppressed by  $>97\%$  on flat and  $>99\%$  on the anodized porous PDMS-infused steel substrates. The immobilized low-surface-tension PDMS lubricant stably present on the UV-grafted and infused substrates, as shown by the thin-film interference pattern in Figure 5d,e,j, introduces an additional liquid–liquid interface, which effectively eliminates the adhesion of both types of bacteria forming biofilm resistive coating.

Next, the UV-grafting approach was applied on the bare, UV-grafted, and PDMS-infused scalpel blades to examine the adhesion of both *E. coli* and *S. aureus* in a medium. After sterilization by dipping the blades in 70 vol% ethanol solution for a few seconds and drying them at ambient atmosphere, the blades were dipped in a solution of medium containing  $\approx 8 \times 10^8$  cells mL<sup>-1</sup> ( $OD_{600\text{ nm}} \approx 1.000$ ) bacteria. The blades were kept for 1 min in the bacterial solution, then withdrawn and rinsed in a cuvette with bacterial medium to remove unbound bacteria, that is, from the droplets that pinned to the blade surface. The cuvette with rinsed bacteria was then measured by UV–Vis spectroscopy at  $\lambda = 600$  nm ( $OD_{600\text{ nm}}$ ), and the results are summarized in Figure 5m,n.<sup>[49]</sup> The amount of remnant bacteria was reduced from bare to UV-grafted and PDMS-infused blades. Previously, we have shown that deposition of sub-micrometer-scale rough tungsten oxide (WO<sub>3</sub>) film on scalpel blades followed by their further modification to a SLIPS can prevent bacterial biofilm adhesion due to the presence of the immobilized liquid layer.<sup>[10g]</sup> This was attributed to the inability of the bacteria to attach to the lubricant surface as any toxic effects of the lubricant on the bacteria had been ruled out. However, the WO<sub>3</sub> deposition process is complex, the kinetics is slow and not applicable on carbon grade steel due to severe corrosion, while the surface modification required the use of short, fluorinated molecules as well as a fluorinated lubricant

both are barely suitable for biomedical applications. Here, the PDMS-infused surfaces have been UV-grafted and infused on bare scalpel blades by a one-pot process using biocompatible silicon oil as both a surface modifier and lubricant.

Immediately after the rinse in the bacterial medium, the incision of the agar plate was performed to determine the number of bacteria that remain on the blade even after extensive rinse, that is, bacteria that strongly adhere to the blade surface. The agar plates were then incubated at 37 °C for 24 h allowing bacterial growth, and the results are presented in Figure 5m,n, top inset images. The number of adherent bacteria to the PDMS-infused scalpels is  $\approx 60\%$  lower for *S. aureus* and  $\approx 50\%$  for *E. coli* compared to plain blades. Furthermore, there is a substantial difference between plain and UV-grafted or PDMS-infused blades in both steel grades. The bacterial biofilm grown from all plain scalpels is even and continuous over the entire incision length (Figure 5m,n, left petri plates in the inset images). On the contrary, UV-grafted and, in particular, PDMS-infused blades display a patchy growth of bacterial biofilms with a thicker grown area at the beginning of the incision. After  $\approx 2$  cm, the biofilms rupture, and only a few individual colonies are observed. The latter indicates that the adhesion of the bacteria is considerably weaker in both UV-grafted and PDMS-infused blades, since the applied friction between the soft agar gel and scalpel blade is sufficient enough to remove the attached bacteria almost completely, which does not occur on plain blades.

### 3. Conclusion

In this study, we introduce a one-pot approach to adopt a surface of virtually any solid substrate into lubricant-infused gaining the material surface superior repellent characteristics. We demonstrate that PDMS or silicone oil, the most common silicone material, grafts to a substrate when illuminated by UV light, simultaneously serving as a reducing surface energy agent and infusing lubricant. The approach was applied to various substrates including metals, metal oxides, and ceramics with surface morphologies from flat to rough. The proposed approach is simple to implement, rapid, non-toxic, environmentally friendly, easily scalable, and low-cost, yet forms a stable lubricant-infused slippery coating. Furthermore, the process does not require pre- or harsh treatment conditions making it suitable to apply in industrial, medical, and other real-life applications. The key advantage of our approach is that micro- or micro/nano- surface structuring is not required. The latter thus eliminates the main complexity of SHS, which is an intrinsic mechanical weakness associated with rough surfaces, yet increases the resistance of the material to corrosion and fouling. Indeed, the addition of surface roughness through anodization and subsequent grafting of the surface with PDMS leads to superhydrophobicity. The latter further increases the corrosion resistance, broadens the passivation range, while the infusion of the SHS with silicone oil for creating a lubricant-infused slippery surface, further reduces the corrosion current density, and increases the corrosion potential. However, the structuring processes may apply harsh conditions on the material and are not always applicable for various substrates reducing the overall

mechanical durability of the material. Therefore, a compromise between mechanical and repellent characteristics should be considered for every particular application.

Due to the biocompatibility of silicone-based compounds, the UV-grafted process was examined on plain medically applicable substrates that display enhanced corrosion resistance, reduced friction, as well as excellent blood and bacterial adhesion repellency. The latter emphasizes that the surface properties of bare medical devices can be substantially modified without deteriorating their mechanical robustness. Furthermore, the UV-grafted medical instruments were sterilized by a brief rinse in 70 vol% ethanol solutions and then were used several times without showing any degradation in their repelling characteristics. The procedure was applied on surgical grades steel scalpels that allowed to cut both soft and hard crosslinked elastomers more accurately. Furthermore, carbon steel, which is used frequently in medical applications, is prone to corrode almost immediately in saline solutions. When UV-grafted, the same scalpel blade made of carbon steel demonstrated substantial improvement in corrosion resistance. When the same procedure was applied on plain convex glass lenses, the slippery PDMS-infused layer was able to repel blood stains almost completely by passive sliding, allowing a complete field of view without distortion and without compromising the mechanical characteristics of bare lens material. The same trend was also observed for bacterial adhesion, while both Gram-positive and Gram-negative bacteria attach loosely to the UV-grafted and PDMS-infused samples and can be removed by application of weak shear or even by capillary forces. Given all aforementioned advances, we envision that the presented approach will push the development of the UV-grafted PDMS lubricant-infused slippery repellent technology toward a wide range of practical applications.

## 4. Experimental Section

**Materials:** 1 × 3 inch microscope glass slides (VWR, Germany), coverslips (#4, Menzel-Glaser, Germany), quartz slides (1-mm-thick, GVB, Germany), *p*-type Si wafer (μChemicals, Germany), SiO<sub>2</sub>/Si wafer (3 in. Si(100) *p*-type with 100 nm SiO<sub>2</sub>, μChemicals, Germany), 0.5-mm-thick Co foil (99.9%, Advent Research Materials, UK), 1-mm-thick Al sheets (99.95%, Advent Research Materials, UK), 0.2-mm-thickness Mo foil (99.95%, Advent Research Materials, UK), 0.5-mm-thick Ti foil (99.99%, Advent Research Materials, UK), 0.6-mm-thick Cu foil (Marawe, Germany), carbon steel (Bayha, Germany), and MSS with the following nominal composition (wt%): 0.6 to 0.7% C, 12% Cr, ≤ 0.5% Ni, ≤ 0.5% Si, ≤ 1% Mn, ≤ 0.03% P, and ≤ 0.025% S (Swann-Morton, UK) surgical blades #22 were used as substrates. Before surface functionalization, the substrates were cleaned ultrasonically in acetone and ethanol for 10 min and then dried under a stream of N<sub>2</sub>. Silicone oil of 100, 500, and 1000 cSt (*M<sub>w</sub>* = 6, 17.3, and 28 kDa, respectively), toluene, ethanol, and acetone were purchased from Carl Roth, Germany, and used as received.

**Stainless Steel and Ti Anodization:** The electrochemical anodization was performed in a standard two-electrode-cell using LAB/SM 7300 DC power supply (ET System, Germany), 316L grade stainless steel (Advent Research Materials) as an anode, and Pt foil as a cathode. Stainless steel samples were anodized in a two-step procedure as previously reported.<sup>[39]</sup> Briefly, an ethylene glycol solution containing 0.1 M of NH<sub>4</sub>F and 0.2 M H<sub>2</sub>O was used as an electrolyte, and the anodization was performed at 20 °C and at an applied potential of 90 V. The duration of the first step anodization was 20 min. Then, the porous anodic layer was removed using an UP100H ultrasonic processor (Hielscher, Germany) in water for 5 min and dried by a stream of N<sub>2</sub>. Thereafter,

a further anodization step was performed for 10 min. After the second-step anodization, the samples were extensively rinsed with a 20:80 (v/v) water–ethanol mixture and then kept in ethanol until annealed in air at 400 °C for 1 h. Ti foil was anodized according to our previously published procedure.<sup>[30]</sup> Briefly, the Ti foil was anodized in a molten o-H<sub>3</sub>PO<sub>4</sub> electrolyte containing 3 M of NH<sub>4</sub>F for 120 min at an applied potential of 15 V and 100 °C. The “as-anodized” samples were immersed in DI water for 12 h to remove residual electrolytes and finally dried under a stream of N<sub>2</sub>. Well-defined, self-organized Ti nanotubular arrays with a thickness of ≈200 nm were obtained.

**Al Foil Oxidation:** Al sheets were oxidized in boiling water for 10 min to form a rough nanometer-scale pseudoboehmite aluminum oxide layer and then dried under a stream of N<sub>2</sub>.<sup>[38]</sup>

**Surface Functionalization and Lubrication:** The samples were horizontally placed in a Petri dish with a quartz cover. Approximately 20 μL cm<sup>-2</sup> of silicone (PDMS) oil was then dropped to cover the entire sample surface and uniform coverage was achieved by tilting the sample. The samples were illuminated by UV (Hg) lamp at 400 W (Noblelight DQ2523, Heraeus, Germany). The emission maxima of this lamp are in the UV range, that is, λ = 320 and 370 nm. The working distance between the lamp and the sample was 15 cm. The UV light power density was measured using a 1830-C Newport optical power meter equipped with a 818-UV/DB optical power detector and 1% Newport ND filter. The power density at the working distance is ≈50 mW cm<sup>-2</sup>. To measure the WCA and hysteresis on UV-grafted PDMS layers, the remnant oil was dissolved by extensive rinsing in toluene, and then dried under a stream of N<sub>2</sub>.

**Scalpel Blade and Glass Lens Functionalization:** To form lubricant-infused slippery scalpels, sterile medical scalpel blades #22 made of i) carbon steel (Bayha, Germany) and ii) MSS (Swann-Morton, UK) were placed horizontally in a glass Petri dish with a quartz cover. The silicone oil was dropped on the blade surface and then the samples were illuminated by a UV lamp for 30 min. The procedure was repeated on every scalpel side. To form UV-grafted PDMS surfaces, the silicone oil was dissolved by an extensive rinse in toluene. The same procedure was also applied on soda-lime, double convex glass optical lenses of 50 mm in diameter.

**Morphology and Physicochemical Characterization:** For morphological characterization, a field-emission scanning electron microscope (Hitachi FE-SEM S4800) was used equipped with energy-dispersive X-ray spectroscopy (EDAX, Genesis). The composition and the chemical state of the films were characterized using XPS (PHI 5600, US), and the spectra were shifted according to the C 1s signal at 284.8 eV, and the peaks were fitted by MultiPak software. Depth profiling was carried out using the instrument's Ar<sup>+</sup> sputter source operated at 3 kV and 15 nA, rastered over a 3 × 3 mm<sup>2</sup> area at a sputtering angle of 45° to the surface normal. Sputter steps of 1 min were repeated till the Si substrate. The atomic composition was determined between consecutive sputtering intervals, by evaluating the photoelectron peak area, using MultiPak processing software. The sputtering rate was calibrated using commercial Si/SiO<sub>2</sub> wafers (3 in. Si(100) *p*-type with 100 nm SiO<sub>2</sub>, μChemicals, Germany) and found as 2 nm min<sup>-1</sup>.

**ToF-SIMS Measurements:** Positive and negative static SIMS measurements were performed on a ToF-SIMS 5 spectrometer (ION-TOF, Münster). The samples were irradiated by a pulsed 25 keV Bi<sub>3</sub><sup>+</sup> liquid-metal ion beam. Spectra were recorded in high mass-resolution mode (*m*/Δ*m* > 8000 at <sup>29</sup>Si). The beam was electrostatically bunched down to 25 ns to increase the mass resolution and raster-scanned over a 125 × 125 μm<sup>2</sup> area. The primary ion dose density was kept at ≈5 × 10<sup>11</sup> ions × cm<sup>-2</sup> ensuring static conditions. Signals were identified using the accurate mass as well as their isotopic pattern and profile. Negative depth profiles are recorded in dual beam mode with a pulsed 25 keV Bi<sup>+</sup> liquid-metal ion beam (bunched down to <0.8 ns) for spectra generation and a 500 eV Cs<sup>+</sup> ion beam for sputter-removal on a 50 × 50 μm<sup>2</sup> area in the center of the 300 × 300 μm<sup>2</sup> sputter crater. Signals are identified according to their isotopic pattern as well as to their exact mass. Spectra are calibrated to CH<sub>2</sub><sup>-</sup>, C<sub>2</sub><sup>-</sup> (negative polarity) and C<sup>+</sup>, CH<sup>+</sup>, CH<sub>2</sub><sup>+</sup>, CH<sub>3</sub><sup>+</sup>, and C<sub>2</sub>H<sub>3</sub><sup>+</sup> (positive polarity) and a Poisson correction is used.

**Contact Angle Measurements:** The contact-angle measurements were performed by a contact angle measurement system (DSA100, Kruss, Germany) at room temperature. The droplet volume for

the measurements was 10  $\mu\text{L}$ , unless otherwise specified, and the macroscopic droplet profile was captured on camera. The droplet profile was fitted by a drop shape analysis computer program provided by the manufacturer. Contact-angle hysteresis was measured by increasing and decreasing the droplet volume and video recording to determine the advancing and receding contact angles. All contact angle values specified in the text were averaged by at least 3 independent measurements.

**Ellipsometric Measurements:** The thickness of PDMS layers was determined with a phase-modulated ellipsometer equipped with a 633 nm He–Ne laser source (Picometer Ellipsometer; Beaglehole Instruments, New Zealand). To achieve sufficient sensitivity for the detection of thin silicone layers, angle scans were performed around the Brewster angle of Si (i.e., 76°)<sup>[50]</sup> from 70 to 80° at a step width of 1° at three different positions of the sample surface. Angle-resolved data from ellipsometry were fitted assuming a 4-layer model by refractive indices of  $n_{\text{air}} = 1.00$ ,  $n_{\text{PDMS}} = 1.403$ ,  $n_{\text{SiO}_2} = 1.457$ ,  $n_{\text{Si}} = 3.4$ , and  $k_{\text{Si}} = 0.03$  for air, PDMS layers, native silicon oxide, and silicon wafer, respectively, while a plane Si wafer (with native oxide layer) was used as reference.

**Corrosion Measurements:** The electrochemical polarization curves were measured in a standard three-electrode-cell using an IM6 electrochemical workstation (Zahner-Elektrik, Germany) and analyzed by the instrument's electrochemical software. Bare stainless steel, anodized stainless steel with grafted PDMS layer (superhydrophobic), anodized slippery stainless steel with grafted and lubricated PDMS were used as working electrodes. Besides, pure copper and pure aluminum substrates were analyzed with bare, UV-grafted, and infused by PDMS oil of 500 cSt viscosity. The electrochemical tests were carried out in a standard 3.5 wt% NaCl aqueous solution as corrosion medium. The cathode was a Pt electrode (20  $\times$  20 mm), the reference electrode was an Ag/AgCl leakless (3.5 m KCl) reference electrode (ET072 eDAQ), and the scanning rate was fixed to 3 mV s<sup>-1</sup>. The potentiodynamic polarization curves were started at -300 mV versus the OCP. In the anodic direction, the polarizations were performed up to 1.6 V for the AISI 316L grade stainless steel; 1.2 V for the pure Al, and 1.0 V for the pure Cu substrates. The calculation of the percentage IE of the corrosion current was performed as follows:  $\text{IE} = ((i_0 - i_c)/i_0) \times 100\%$ , where  $i_0$  is the corrosion current of the bare sample, and  $i_c$  is the corrosion current of the coated sample (UV-grafted or lubricant-infused). These values were obtained by the Tafel method after performing the polarization curves.

**Blood Attachment Experiments:** Fresh pig blood was generously provided by Unifleisch GmbH (Erlangen, Germany). Sodium citrate (0.5 vol%) was added to the blood before receipt (at the lab facility) to prevent blood clotting. It was rotated on a mixer at 20 rpm to homogenize the contents before sampling.

**Bacterial Stock Preparation:** The wild-type bacterial strain *E. coli* DH 5 alpha strain and *S. aureus* were used. The stock culture was generated from an agar stock plate, from which one or two colonies were transferred to the growth medium. All cultures were incubated overnight at 37 °C in 5 mL of Tryptic Soy Broth growth medium (Becton Dickinson, Heidelberg) and kept shaking continuously in an orbital shaker at a speed of 150 turns min<sup>-1</sup>. The concentration of bacteria was measured by UV–Vis spectroscopy at a wavelength of 600 nm wavelength (OD<sub>600 nm</sub>) versus pure medium (control) and calculated according to the equation:  $1.000 \text{ OD}_{600 \text{ nm}} = 8 \times 10^8 \text{ CFU mL}^{-1}$ .<sup>[49]</sup>

**Bacterial Biofilm Adhesion:** Bare polished, anodized (hydrophilic), PDMS UV-grafted (hydrophobic), and slippery (lubricant-infused) stainless steel samples were placed horizontally in a 10 cm petri dish with 3 samples of 2 cm<sup>2</sup> per dish. The *E. coli* and *S. aureus* stock solution was diluted to OD<sub>600 nm</sub> = 0.55 by growth medium. Thereafter, the surface of each sample was covered with 900  $\mu\text{L}$  of the bacteria solution. Immediately following inoculation, all samples were incubated at 37 °C for 24 h to allow proper biofilm growth. Triplicates were done for both (*E. coli* and *S. aureus*) infused samples and non-infused controls. Biofilm coverage was analyzed by staining all samples in Neisser's solution II (Crystal violet, Carl Roth, Germany). This was followed by gentle rinsing in DI water to remove excess stain and then air-dried. Images were captured by confocal microscopy (Leica, Wetzlar), bright-field optical microscopy (Nikon, Japan), and SEM microscopy (Hitachi, Japan, without any additional pre-treatment using a reduced working voltage).

**Bacterial Adhesion to Medical Scalpel Blades:** Bacteria adhesion was achieved by dipping untreated or treated scalpel blades into a stock solution containing *E. coli* or *S. aureus* at OD<sub>600 nm</sub>  $\approx$  1.000 in Tryptic Soy Broth culture medium. The scalpel blades were first kept submerged for 1 min in the *E. coli* or *S. aureus* solution then withdrawn and rinsed in 4 mL of the culture medium. The washing solution was measured by UV–vis spectroscopy at  $\lambda = 600 \text{ nm}$ . After the wash, the scalpels were used to scissor the agar in the petri dishes, which were then incubated for 24 h at 37 °C. The scalpel blades were sterilized by a brief rinse in 70% ethanol aqueous solution between the subsequent submersions in different bacterial cultures. Three replicates per treatment were used. Statistical analysis (two-tailed t-test) was performed to determine the statistical significance of bacterial resistance.

**Theoretical Calculations:** The program ORCA 4.1.1 was used for all calculations.<sup>[51]</sup> Geometry optimizations were performed on a truncated model for PDMS: Me<sub>3</sub>Si–O–SiMe<sub>2</sub>–O–SiMe<sub>3</sub>. The bond of interest was homolytically broken, and the two resulting radical fragments ( $S = 1/2$  each) were independently optimized. The true minima were confirmed by calculating vibrational frequencies showing no negative values. M06-2X functional<sup>[52]</sup> and def2-TZVP basis sets<sup>[53]</sup> for all atoms were used. To speed up the calculations, RIJCOSX approximation with def2/J auxiliary basis sets<sup>[54]</sup> were employed. When calculating bond-dissociation enthalpy  $DH_{298}^0$ , zero-point energy and thermal energy corrections were applied routinely.

## Supporting Information

Supporting Information is available from the Wiley Online Library or from the author.

## Acknowledgements

A.B.T. and L.H.P. contributed equally to this work. Financial support was granted by the DFG and DFG Cluster of Excellence EAM. A.B.T. acknowledges the Emerging Talents Initiative (ETI) of Friedrich-Alexander-University (Grant number 5500102) and thanks the DFG (Grant number 442826449; SCHM 1597/38-1 and FA 336/13-1) for their financial support. M.M.K. confirms financial support from DFG (Grant number KH 279/6-1) and FAU Erlangen-Nuremberg. The authors thank Ms. Vanessa Goetz and Ms. Helga Hildebrand for their help with ellipsometric, XPS, and ToF-SIMS measurements. A patent of this research has been filed with the European Patent Office, Munich.

Open access funding enabled and organized by Projekt DEAL.

## Conflict of Interest

The authors declare no conflict of interest.

## Data Availability Statement

Data available on request from the authors.

## Keywords

anti-biofouling, blood-repellent coating, corrosion resistance, lubricant-infused slippery surfaces, polydimethylsiloxane

Received: February 1, 2021

Revised: March 6, 2021

Published online:

- [1] M. Liu, S. Wang, L. Jiang, *Nat. Rev. Mater.* **2017**, *2*, 17036.
- [2] P.-G. de Gennes, F. Brochard-Wyart, D. Quéré, in *Capillarity and Wetting Phenomena: Drops, Bubbles, Pearls, Waves* (Eds: P.-G. deGennes, F. Brochard-Wyart, D. Quéré), Springer, New York **2004**, p. 153.
- [3] a) J. R. Davis, in *Corrosion: Understanding the Basics* (Ed: J. R. Davis), ASM International, Ohio **2000**, p. 1; b) G. Koch, in *Trends in Oil and Gas Corrosion Research and Technologies* (Ed: A. M. El-Sherik), Woodhead Publishing, Boston **2017**, p. 3.
- [4] L. Jackson, *Marine Biofouling & Invasive Species: Guidelines for Prevention and Management, Global Invasive Species Programme*, Global Invasive Species Programme, UNEP Regional Seas Programme, Nairobi, Kenya **2008**.
- [5] M. P. Schultz, J. A. Bendick, E. R. Holm, W. M. Hertel, *Biofouling* **2011**, *27*, 87.
- [6] G. B. Hwang, K. Page, A. Patir, S. P. Nair, E. Allan, I. P. Parkin, *ACS Nano* **2018**, *12*, 6050.
- [7] a) V. Jokinen, E. Kankuri, S. Hoshian, S. Franssila, R. H. A. Ras, *Adv. Mater.* **2018**, *30*, 1705104; b) A. Lafuma, D. Quéré, *Nat. Mater.* **2003**, *2*, 457.
- [8] A. Marmur, *Langmuir* **2004**, *20*, 3517.
- [9] a) A. Lafuma, D. Quéré, *Europhys. Lett.* **2011**, *96*, 56001; b) T.-S. Wong, S. H. Kang, S. K. Y. Tang, E. J. Smythe, B. D. Hatton, A. Grinthal, J. Aizenberg, *Nature* **2011**, *477*, 443.
- [10] a) A. K. Epstein, T.-S. Wong, R. A. Belisle, E. M. Boggs, J. Aizenberg, *Proc. Natl. Acad. Sci. USA* **2012**, *109*, 13182; b) X. Hou, J. Li, A. B. Tesler, Y. Yao, M. Wang, L. Min, Z. Sheng, J. Aizenberg, *Nat. Commun.* **2018**, *9*, 733; c) C. Howell, T. L. Vu, J. J. Lin, S. Kolle, N. Juthani, E. Watson, J. C. Weaver, J. Alvarenga, J. Aizenberg, *ACS Appl. Mater. Interfaces* **2014**, *6*, 13299; d) D. C. Leslie, A. Waterhouse, J. B. Berthet, T. M. Valentin, A. L. Watters, A. Jain, P. Kim, B. D. Hatton, A. Nedder, K. Donovan, E. H. Super, C. Howell, C. P. Johnson, T. L. Vu, D. E. Bolgen, S. Rifai, A. R. Hansen, M. Aizenberg, M. Super, J. Aizenberg, D. E. Ingber, *Nat. Biotechnol.* **2014**, *32*, 1134; e) J. Li, T. Kleintschek, A. Rieder, Y. Cheng, T. Baumbach, U. Obst, T. Schwartz, P. A. Levkin, *ACS Appl. Mater. Interfaces* **2013**, *5*, 6704; f) B. R. Solomon, S. B. Subramanyam, T. A. Farnham, K. S. Khalil, S. Anand, K. K. Varanasi, in *Non-Wettable Surfaces: Theory, Preparation and Applications*, The Royal Society of Chemistry, London **2017**, p. 285; g) A. B. Tesler, P. Kim, S. Kolle, C. Howell, O. Ahanotu, J. Aizenberg, *Nat. Commun.* **2015**, *6*, 8649; h) N. Vogel, R. A. Belisle, B. Hatton, T.-S. Wong, J. Aizenberg, *Nat. Commun.* **2013**, *4*, 2176; i) X. Hou, *Natl. Sci. Rev.* **2019**, *7*, 9; j) X. Hou, *Adv. Mater.* **2016**, *28*, 7049.
- [11] A. B. Tesler, Z. Sheng, W. Lv, Y. Fan, D. Fricke, K.-C. Park, J. Alvarenga, J. Aizenberg, X. Hou, *ACS Nano* **2020**, *14*, 2465.
- [12] Z. Sheng, J. Zhang, J. Liu, Y. Zhang, X. Chen, X. Hou, *Chem. Soc. Rev.* **2020**, *49*, 7907.
- [13] a) S. Amini, S. Kolle, L. Petrone, O. Ahanotu, S. Sunny, C. N. Sutanto, S. Hoon, L. Cohen, J. C. Weaver, J. Aizenberg, N. Vogel, A. Miserez, *Science* **2017**, *357*, 668; b) C. Howell, A. Grinthal, S. Sunny, M. Aizenberg, J. Aizenberg, *Adv. Mater.* **2018**, *30*, 1802724; c) P. Kim, T.-S. Wong, J. Alvarenga, M. J. Kreder, W. E. Adorno-Martinez, J. Aizenberg, *ACS Nano* **2012**, *6*, 6569; d) K.-C. Park, P. Kim, A. Grinthal, N. He, D. Fox, J. C. Weaver, J. Aizenberg, *Nature* **2016**, *531*, 78.
- [14] R. Deng, T. Shen, H. Chen, J. Lu, H.-C. Yang, W. Li, *J. Mater. Chem. A* **2020**, *8*, 7536.
- [15] M. Hasanzadeh Kafshgari, W. H. Goldmann, *Nano-Micro Lett.* **2020**, *12*, 22.
- [16] X. Yao, Y. Hu, A. Grinthal, T.-S. Wong, L. Mahadevan, J. Aizenberg, *Nat. Mater.* **2013**, *12*, 529.
- [17] C. Shillingford, N. MacCallum, T.-S. Wong, P. Kim, J. Aizenberg, *Nanotechnology* **2013**, *25*, 014019.
- [18] a) S. Sunny, G. Cheng, D. Daniel, P. Lo, S. Ochoa, C. Howell, N. Vogel, A. Majid, J. Aizenberg, *Proc. Natl. Acad. Sci. USA* **2016**, *113*, 11676; b) J. Wang, L. Wang, N. Sun, R. Tierney, H. Li, M. Corsetti, L. Williams, P. K. Wong, T.-S. Wong, *Nat. Sustain.* **2019**, *2*, 1097.
- [19] P. Kim, M. J. Kreder, J. Alvarenga, J. Aizenberg, *Nano Lett.* **2013**, *13*, 1793.
- [20] D. Paulssen, S. Hardt, P. A. Levkin, *ACS Appl. Mater. Interfaces* **2019**, *11*, 16130.
- [21] Y. Yao, T. Y. Zhao, C. Machado, E. Feldman, N. A. Patankar, K.-C. Park, *Proc. Natl. Acad. Sci. USA* **2020**, *117*, 6323.
- [22] H. Fiedler, R. Kallenborn, J. d. Boer, L. K. Sydnes, *Chem. Int.* **2019**, *41*, 4.
- [23] a) M. Andriot, S. H. Chao, A. Colas, S. Cray, F. de Buyl, J. V. DeGroot, A. Dupont, T. Easton, J. L. Garaud, E. Gerlach, F. Gubbels, M. Jungk, S. Leadley, J. P. Lecomte, B. Lenoble, R. Meeks, A. Mountney, G. Shearer, S. Stassen, C. Stevens, X. Thomas, A. T. Wolf, in *Inorganic Polymers* (Eds: R. De Jaeger, M. Gleria), Nova Science Publishers Inc., New York **2007**, pp. 61–161; b) U. Eduok, O. Faye, J. Szpunar, *Prog. Org. Coat.* **2017**, *111*, 124.
- [24] E. Seo, M. R. Seong, J. W. Lee, H. Lim, J. Park, H. Kim, H. Hwang, D. Lee, J. Kim, G. H. Kim, D. S. Hwang, S. J. Lee, *ACS Omega* **2020**, *5*, 11515.
- [25] P. Vondráček, B. Doležel, *Biomaterials* **1984**, *5*, 209.
- [26] H. Teisala, P. Baumli, S. A. L. Weber, D. Vollmer, H.-J. Butt, *Langmuir* **2020**, *36*, 4416.
- [27] a) J. W. Krumpfer, T. J. McCarthy, *Langmuir* **2011**, *27*, 11514; b) S. T. Milner, T. A. Witten, M. E. Cates, *Macromolecules* **1988**, *21*, 2610; c) C.-H. Xue, X. Bai, S.-T. Jia, *Sci. Rep.* **2016**, *6*, 27262; d) L. Chen, S. Park, J. Yoo, H. Hwang, H. Kim, J. Lee, J. Hong, S. Woo, *Adv. Mater. Interfaces* **2020**, *7*, 2000305; e) C. Zhang, Y. Xia, H. Zhang, N. S. Zacharia, *ACS Appl. Mater. Interfaces* **2018**, *10*, 5892.
- [28] a) S. Wooh, N. Encinas, D. Vollmer, H.-J. Butt, *Adv. Mater.* **2017**, *29*, 1604637; b) C. Yang, F. Wang, W. Li, J. Ou, C. Li, A. Amirfazli, *Appl. Phys. A: Mater. Sci. Process.* **2015**, *122*, 1.
- [29] W. A. M. Aarnink, A. Weishaupt, A. van Silfhout, *Appl. Surf. Sci.* **1990**, *45*, 37.
- [30] A. B. Tesler, M. Altomare, P. Schmuki, *ACS Appl. Nano Mater.* **2020**, *3*, 10646.
- [31] J. Liu, L. Ye, S. Wooh, M. Kappl, W. Steffen, H.-J. Butt, *ACS Appl. Mater. Interfaces* **2019**, *11*, 27422.
- [32] a) B. Schnyder, T. Lippert, R. Kötz, A. Wokaun, V.-M. Graubner, O. Nuyken, *Surf. Sci.* **2003**, *532–535*, 1067; b) M. Brinkmann, V. Z. H. Chan, E. L. Thomas, V. Y. Lee, R. D. Miller, N. Hadjichristidis, A. Avgeropoulos, *Chem. Mater.* **2001**, *13*, 967; c) M. Ouyang, R. J. Muisener, A. Boulares, J. T. Koberstein, *J. Membr. Sci.* **2000**, *177*, 177.
- [33] S. Tardio, M.-L. Abel, R. H. Carr, J. E. Castle, J. F. Watts, *J. Vac. Sci. Technol., A* **2015**, *33*, 05E122.
- [34] A. Kaur, P. Chahal, T. Hogan, *IEEE Electron Device Lett.* **2016**, *37*, 142.
- [35] A. J. Pertsin, M. M. Gorelova, V. Y. Levin, L. I. Makarova, *J. Appl. Polym. Sci.* **1992**, *45*, 1195.
- [36] A. Sabata, W. J. van Ooi, H. K. Yasuda, *Surf. Interface Anal.* **1993**, *20*, 845.
- [37] Y. Hashimoto, T. Yamamoto, *Appl. Surf. Sci.* **2017**, *419*, 319.
- [38] A. B. Tesler, T. Sannomiya, A. Vaskevich, E. Sabatani, I. Rubinstein, *Adv. Opt. Mater.* **2018**, *6*, 1800599.
- [39] L. Prado, E. Anastasiou, S. Virtanen, *J. Electrochem. Soc.* **2021**, *168*, 021507.
- [40] A. I. Hochbaum, J. Aizenberg, *Nano Lett.* **2010**, *10*, 3717.
- [41] a) *BS-EN-ISO-7153, Part 1: Metals*, The International Organization for Standardization, **2016**; b) *BS-2982:1992 Specification for Materials and Packaging of Surgical Scalpels with Detachable Blades*, The British Standards Institution, **1992**, p. 10.
- [42] D. Dwivedi, K. Lepková, T. Becker, *RSC Adv.* **2017**, *7*, 4580.

- [43] E. K. Hanson, J. Ballantyne, *PLoS One* **2010**, *5*, e12830.
- [44] G. H. Ballantyne, *Surg. Laparosc. Endosc. Percutan. Tech.* **2002**, *12*, 1.
- [45] T. Okamoto, T. Ohnishi, H. Kawahira, O. Dergachyava, P. Jannin, H. Haneishi, *Signal Image Video Process.* **2019**, *13*, 405.
- [46] F. Tsai, D. Johnson, C. Francis, S.-H. Cho, *J. Biomed. Opt.* **2010**, *15*, 030504.
- [47] *ECDC: Annual Epidemiological Report for 2017*, ECDC, Stockholm **2019**.
- [48] Y. Kovalenko, I. Sotiri, J. V. I. Timonen, J. C. Overton, G. Holmes, J. Aizenberg, C. Howell, *Adv. Healthcare Mater.* **2017**, *6*, 1600948.
- [49] J. A. Myers, B. S. Curtis, W. R. Curtis, *BMC Biophys.* **2013**, *6*, 4.
- [50] J. C. Stewart, M. N. Shelley, N. R. Schwartz, S. K. King, D. W. Boyce, J. W. Erikson, D. D. Allred, J. S. Colton, *Opt. Mater. Express* **2019**, *9*, 4677.
- [51] F. Neese, *ORCA 4.1.1 – Ab Initio, DFT and Semiempirical Electronic Structure Package*, Max-Planck-Institut für Kohlenforschung, Mülheim/Ruhr, Germany.
- [52] Y. Zhao, D. G. Truhlar, *Theor. Chem. Acc.* **2008**, *120*, 215.
- [53] F. Weigend, R. Ahlrichs, *Phys. Chem. Chem. Phys.* **2005**, *7*, 3297.
- [54] F. Weigend, *Phys. Chem. Chem. Phys.* **2006**, *8*, 1057.